Available online at www.sciencedirect.com
ScienceDirect
Trans. Nonferrous Met. Soc. China 27(2017) 55−62
Transactions of Nonferrous Metals Society of China
www.tnmsc.cn

Corrosion pathways in aluminium alloys

U. DONATUS[1,2], G. E. THOMPSON[1], J. A. OMOTOYINBO[2], K. K. ALANEME[2], S. ARIBO[2], O. G. AGBABIAKA[2]

1. School of Materials, The University of Manchester, Manchester M13 9PL, England, UK;
2. Department of Metallurgical and Materials Engineering, Federal University of Technology, Akure, PMB 704, Akure, Ondo State, Nigeria

Received 7 March 2016; accepted 28 June 2016

Abstract: The corrosion pathways in AA2024-T3, AA5083-O and AA6082-T6 alloys have been investigated. The objective of the investigation is to further the understanding of the complex localised corrosion mechanism in aluminium alloys. The investigation was carried out by examining the corroded surfaces of the alloys after potentiodynamic polarization tests in a 3.5% NaCl solution with the aid of a scanning electron microscope, and by analysing the flow of anolyte solution using the scanning vibrating electrode technique. The results revealed that the overall corrosion pathways in the alloys are distinctively different and are influenced by the flow of anolyte solution. Also revealed, was the fact that corrosion propagates in two ways (particularly in the AA5083-O and AA6082-T6 alloys): an overall pathway in the corrosion front (filiform-like pathway in the AA5083 alloy and organized linear pathways in AA6082 alloy); and the crystallographic channelling along the ⟨100⟩ directions. These are dependent on the grain distinct features of the AA5083-O and AA6082-T6 alloys and are not influenced by the presence of coarse second phase particles in these alloys, compared with the AA2024-T3 alloy, where the corrosion pathways are more dependent on the presence of second phase particles and grain boundary character.

Key words: corrosion front pathway; crystallographic channelling; anolyte flow; aluminium alloy

1 Introduction

The localized corrosion behaviour of aluminium alloys has been widely studied, particularly in the last two decades, using various characterization tools and techniques. Electrochemical techniques do not give a true representation of the localized corrosion kinetics and morphology. ZHANG and FRANKEL [1] argued this in the past, where they stated that there are problems associated with the use of electrochemical techniques for the study of localized corrosion in high strength aluminium alloys because 1) it is difficult to measure the active area during localized corrosion, 2) some of the anodic currents are used for H_2 evolution and, thus, the measured current will not be a true representation of the corrosion kinetics, and 3) the use of electrochemical techniques in the study of localized corrosion under open circuit conditions is impossible. Thus, other techniques have been used to give more information on the morphology and kinetics of localized corrosion in addition to electrochemical techniques. Such techniques and tools include foil penetrant technique [1], confocal laser scanning microscopy [2], 3-D tomography and reconstruction [3−5], Auger electron spectroscopy and Rutherford backscattering [6], scanning Kelvin probe force microscopy and atomic force microscopy [7−9], and scanning electron and transmission electron microscopies [3,5,10−13].

Reports about the influence of second phase particles on the localized corrosion behaviour of aluminium alloys abound in the literature [10,12−21]. Second phase particles like the Al_2CuMg, Al_3Mg_2, Mg_2Si, and $MgZn_2$ are anodic to the Al matrix and corrode preferentially with respect to the surrounding Al matrix. The behaviour of the *S*-phase (Al_2CuMg) is a bit more complicated: firstly, the Mg and Al components are leached out to leave behind a spongy Cu remnant which makes it eventually cathodic to the Al matrix and causes the dissolution of the adjacent Al matrix. On the other hand, there are second phase particles such as Al_2Cu (θ), AlFeMnSi, AlCuFeMn, AlCuFeSi, and $(Al,Cu)_x(Fe,Mn)_ySi$ particles which are mostly cathodic to the Al matrix and cause peripheral trenches of the

Corresponding author: U. DONATUS; Tel: +44-7442269383; Fax: +44(0)1613064865; E-mail: uyimedonatus@yahoo.com
DOI: 10.1016/S1003-6326(17)60006-2

surrounding Al matrix adjacent to these second phase particles.

The morphological characterization of the localized corrosion behaviour of Al alloys has been mostly linked to the behaviours or nature of these second phase particles [10,12,13,15−21]. However, few authors have considered other factors. LUO et al [22] considered the influence of grain stored energy on the intergranular corrosion pathway in an AA2024T3 alloy and revealed that the intergranular dissolution was more on the grain with higher stored energy at the grain boundary between the two grains. Still on grain boundary character, KIM et al [23] investigated the effect of grain boundary character distribution on the intergranular corrosion susceptibility of pure Al alloy in different concentrations of HCl solution. It was reported that low angle grain boundaries were more resistant to intergranular corrosion compared with twin boundaries and random boundaries in all the concentrations of HCl used in the study, and this was particularly noted at lower concentrations of HCl solution. At HCl concentrations of 16% and 8%, twin boundaries were observed to be more resistant to intergranular corrosion compared with random boundaries. In addition, TAN and ALLEN [24] reported that grain angle boundaries less than 20° tend to be more resistant to corrosion. MINODA and YOSHIDA [25] also made similar findings while investigating the intergranular corrosion behaviour of an extruded AA6061 aluminium alloy in accordance with the ISO 11846 method. It was observed that the surface of the extruded AA6082 alloy, which has recrystallized grains with random high angle boundaries, was more susceptible to intergranular corrosion compared with the centre plane of the extruded alloy. The susceptibility to intergranular corrosion was attributed to the formation of precipitate free zones, and the formation of the precipitate free zones was related to the presence of high angle boundaries. This was confirmed by cold rolling and recrystallizing the grains of the centre plane; and random high angle grain boundaries and heavy intergranular corrosion were observed afterward. However, more recent findings have shown that finer grained regions of aluminium alloys are more resistant to corrosion in near neutral pH media and are more prone to corrosion in low pH (acidic) media [10,26,27] such as the medium MINODA and YOSHIDA used in conducting their investigation. Higher kinetics of passive film formation and “cleaner” grain boundaries were attributed to the better corrosion resistance of finer grained regions in near neutral environment [26,27].

In spite of all this work on the influence of grain boundary character, grain stored energy, and second phase particles on the localized corrosion behaviour of aluminium alloys, the localized corrosion behaviour of aluminium alloys is far from being fully understood and arguments still exist. This is in addition to the fact that information on the effect of grain distinct crystallograhic details of the alloys and flow of anolyte solution on the localized corrosion behaviour of aluminium alloys is rare to find in literature. Therefore, the focus of this work is to investigate the corrosion pathways, particularly within the grains of AA2024-T3, AA5083-O and AA6082-T6 alloys after polarization tests. The investigation is based on the observed corrosion morphologies in the grains of the alloys (using scanning electron microscopy, after potentiodynamic polarization tests) and the observation of anolyte solution flow during a galvanic corrosion test between AA2024-T3 and mild steel alloys using the scanning vibrating electrode technique (SVET).

2 Experimental

Three different aluminium alloys, namely AA2024-T3, AA5083-O and AA6082-T6 aluminium alloys were used in this study. The compositions of the alloys are presented in Table 1. The AA2024-T3 alloy was obtained from Airbus whilst the AA5083-O and AA6082-T6 alloys were obtained from the Welding Institute, UK.

Table 1 Compositional analysis of major alloying elements in AA2024-T3, AA5083-O, and AA6082-T6 aluminium alloys used in this study (mass fraction, %)

Alloy	Mg	Si	Mn	Fe	Zn	Cu	Ti	Cr
AA2024-T3	1.2−1.8	0.5	0.3−0.9	0.5	0.24	3.8−4.9	0.15	0.1
AA5083-O	3.92	0.03	0.44	0.23	0.01	−	−	−
AA6082-T6	0.74	0.44	0.40	0.33	0.05	−	−	−

Samples from the alloys were sequentially polished up to 1 μm surface finish using SiC papers and a 1 μm diamond paste with an alcohol based lubricant. The polished samples were then degreased in an ultrasonic bath for 15 min and rinsed in deionized water before drying in a cool air stream. The dried samples were then coated with Lacquer 45 whilst exposing a 1 cm^2 surface area prior to potentiodynamic polarization tests.

Potentiodynamic polarization tests were conducted in a naturally aerated 3.5% NaCl solution using a Modulab potentiostat. A 3-electrode cell comprising the workpiece, a saturated calomel electrode (as the reference electrode) and a platinum electrode (as the counter electrode) was used for the polarization tests. Polarized samples were immediately rinsed in deionized

water, dried and stored in a desiccator until further investigations were required.

A corrosion immersion test for an AA2024-T3/mild steel couple was also carried out using a Swansea University manufactured scanning vibrating electrode technique (SVET) machine. The mild steel plate used in the SVET immersion test was a Fed Steel QQ-S-698 having nominal composition of 0.25%−0.6% Mn, 0.13% C, 0.04% P and 0.05% S (mass fraction), and was obtained from AGAR SCIENTIFIC ELEKTRON in a rolled condition. The immersion test was conducted at a solution temperature of (45±2) °C in a naturally aerated 3.5% NaCl solution. The experimental set-up for the SVET immersion test is as detailed in Ref. [28].

Microstructural examination of the corroded samples from the potentiodynamic polarization tests and SVET immersion test were carried out using a ZEISS Ultra 55 scanning electron microscope and a ZEISS AXIO optical microscope.

3 Results and discussion

This section presents the scanning electron micrographs of potentiodynamically polarized samples of AA2024-T3, AA5083-O, and AA6082-T6 aluminium alloys, and the SVET results of the galvanic interaction between AA2024-T3 and mild steel alloys. The purpose is to compare the varying morphological features in these alloys after the alloys have undergone localized corrosion in a bid to understand the corrosion front pathways in the alloys.

Figure 1 displays scanning electron micrographs of the AA2024-T3 alloy after it has been potentio-dynamically polarized in naturally aerated 3.5% NaCl solution. The micrographs show the typical corrosion features in AA2024-T3 alloy: peripheral dissolution/or trenching of the matrix adjacent to the cathodic second phase particles (Figs. 1(a) and (b)), corrosion ring (a characteristic feature of stable pitting) and intergranular attack Fig. 1(c). Also shown in the figure is a pit with crystallographic attack (Fig. 1(d)), arranged in nano-dimension as the attack proceeds beneath the surface.

Displayed in Fig. 2 are micrographs of the AA5083-O alloy after polarization showing clear crystallographic form of corrosion with no influence of second phase particles (Figs. 2(a) and (b)). The morphological features of the corrosion attack in this alloy are solely dependent on grain-specific details of the alloy and not on the second phase particles. Although in certain conditions (open circuit conditions mostly), a sensitized AA5083 alloy which has Al_3Mg_2 (β) phases precipitated at its grain boundaries will exhibit intergranular corrosion caused by the selective dissolution of the active β phases at the grain boundaries. However, the corrosion front pathway in the grains of the alloy after the initiation of corrosion is filiform-like (Fig. 2(b)) but channels along specific crystallographic ⟨100⟩ paths (tunneling or channeling corrosion has long been proven to occur in ⟨100⟩ directions and bounded by {100} planes [29,30]). The corrosion pathway in this alloy is significantly different from that of the

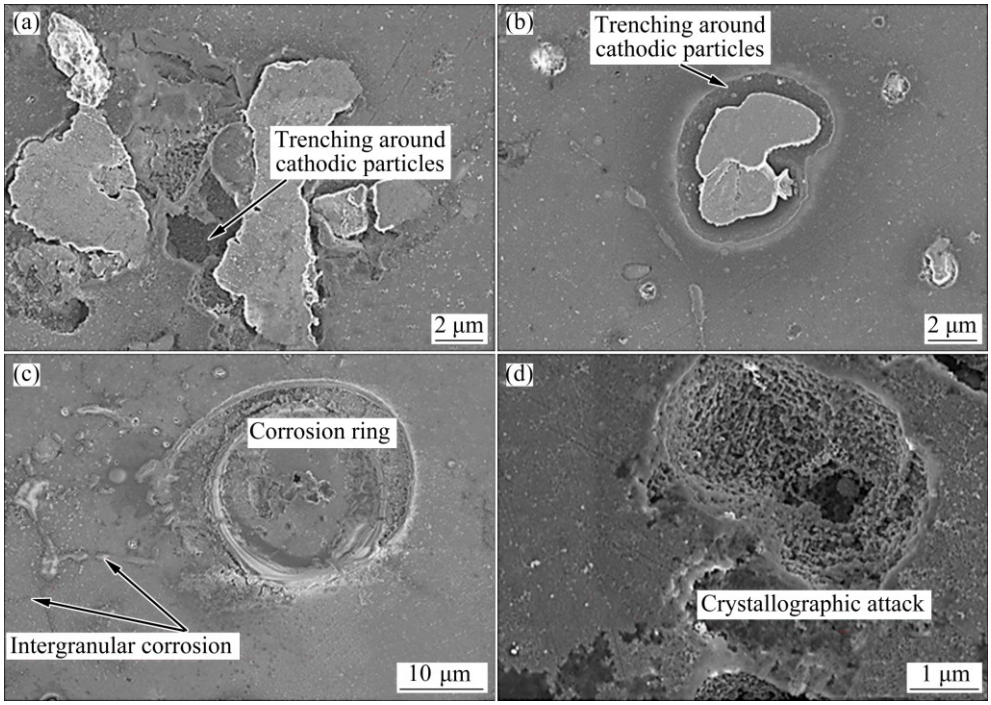

Fig. 1 Scanning electron micrographs of as-polarized AA2024-T3 aluminium alloy displaying trenching around cathodic second phase particles (a, b), corrosion ring and intergranular corrosion (c), and crystallographic corrosion morphology (d)

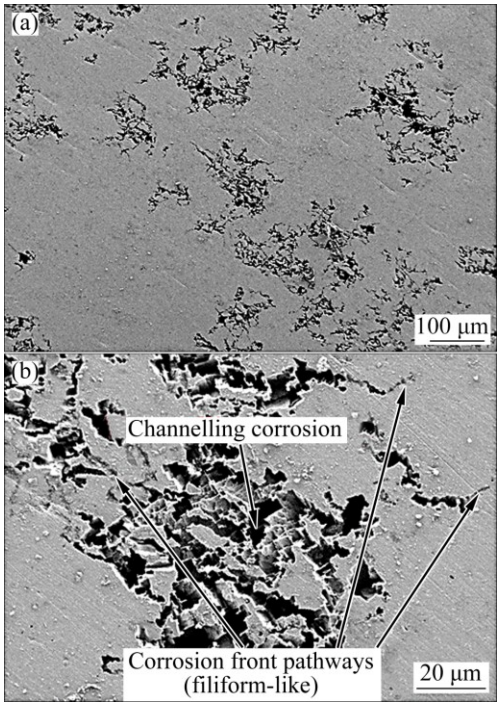

Fig. 2 Scanning electron micrographs of as-polarized AA5083-O aluminium alloy displaying filiform-like corrosion front pathways and channelling form of corrosion: (a) Micrograph of alloy at lower magnification; (b) Micrograph of alloy at higher magnification

AA2024-T3 alloy which is heavily influenced by the presence of coarse precipitates.

In a similar way, the AA6082-T6 alloy does not show particle-induced corrosion morphology as displayed in Figs. 3 and 4 (micrographs of the AA6082-T6 alloy after potentiodynamic polarization). The features are very similar (though with smaller channels (Fig. 4)) compared with those of the AA5083-O alloy. The corrosion front morphology is also crystallographic and channels along the ⟨100⟩ directions. However, unlike the AA5083-O alloy where the corrosion front pathway is mostly filiform-like as displayed in Fig. 2(b), that of the AA6082-T6 alloy is mostly organized and follows more of a defined linear path (see Fig. 3). The crystallographic form of corrosion in these two alloys is primarily dependent on the arrangement and alignment of the grain distinct layers [31] which are parallel to the (100) planes and have more active paths in the ⟨100⟩ directions. For instance, grain *A* in Fig. 3 has the layers that are aligned differently with respect to the corroding surface compared with grain *B*. This is why the corrosion pathway in grain *A* is different from that of grain *B*. This is even more pronounced in Fig. 4, where the channelling corrosion morphology in grain *C* is distinctively different from that of grain *D*; and this is due to different inclinations of the grain distinct layers with respect to the corroding surface. The grain distinct layers [31], which dictate the corrosion pathways in these alloys, are in turn dependent on the thermomechanical history of the alloys.

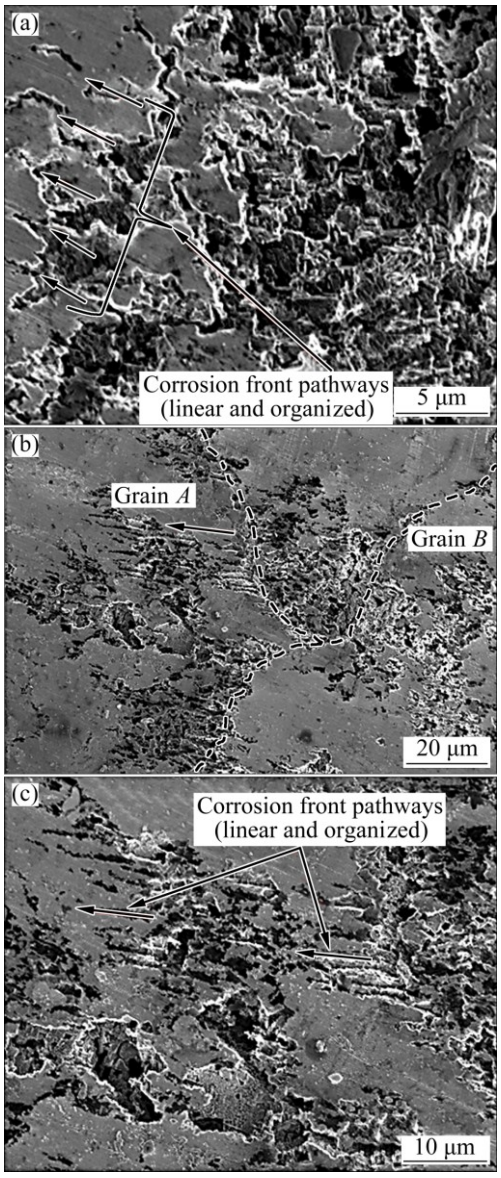

Fig. 3 Scanning electron micrographs of as-polarized AA6082-T6 aluminium alloy displaying linear and organized corrosion front pathways in different zones

The AA5083 and AA6082 alloys have coarse Fe-rich type particles (such as the AlFeMnSi and AlFeMn particles) [10], but these particles rarely influence the corrosion susceptibility and pathways in these alloys. The particles mainly lead to the formation of surface cavities with no further attack often observed. It is the Al_3Mg_2 (in AA5083) and Mg_2Si (in AA6082) phases that cause intergranular corrosion in these alloys; and this occurs in the sensitized states of the alloys in open circuit conditions particularly. In polarized conditions, these alloys exhibit crystallographic forms of corrosion which channels along the ⟨100⟩ directions in

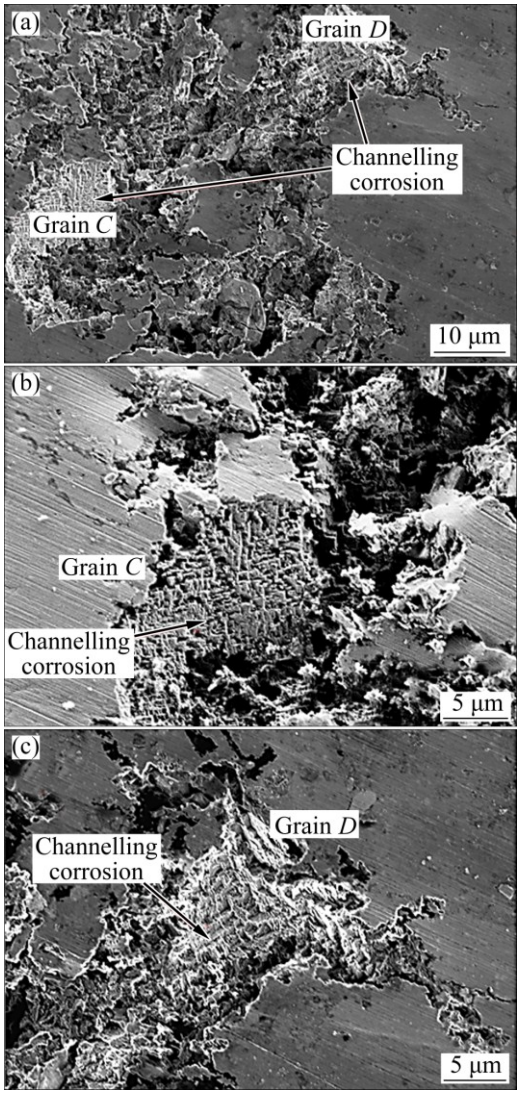

Fig. 4 Scanning electron micrographs of as-polarized AA6082-T6 aluminium alloy displaying different channelling corrosion morphologies in different grains

the grains of the alloys, and these corrosion modes and propagation routes do not appear to be influenced by the presence of second phase particles. On the other hand, the corrosion mode in the AA2024-T3 alloy, both after polarization and in open circuit conditions, is dictated by the presence of coarse precipitates with the cathodic phases, causing the trenching of adjacent Al matrix. However, it is the anodic *S*-phase (Al_2CuMg) that has been heavily linked with stable pitting and intergranular corrosion particularly in regions where there is clustering of the *S*/*θ*-phase particles [12,14,20,32]. The corrosion front pathway after corrosion initiation also appears to be dependent on the crystallographic details of the alloy when viewed at nanoscale (see Fig. 1(d)). It has been reported in recent time that sub-surface features that are linked with the crystallographic details of the grains of aluminium alloys affect the electrochemical responses of aluminium alloys [31]. As earlier stated, the grain distinct crystallographic details are dependent on the extent of prior cold working and heat treatment processes the alloys have been subjected to.

Another important factor to consider is the flow of the anolyte solution. Generally, after the initiation of localized corrosion (such as pitting) in Al alloys, hydrolysis occurs at the pit head to produce H^+ ions and $Al(OH)_3$, which cover the pit and prevents the access of O_2 into the pit. In order to maintain electroneutrality, Cl^- ions drift into the pit head. Thus, inside the pit the pH of the anolyte solution is quite low, making the anolyte solution at the corrosion front acidic and aggressive. Given that the anolyte solution is acidic and aggressive, the direction of flow of this anolyte solution will have significant influence on the corrosion front pathway. The filiform-like corrosion front pathway in the AA5083-O alloy is very much influenced by the flow of the anolyte solution in combination with the channelling path. This is why the corrosion front pathway is not particularly organized. In the case of AA6082-T6 alloy, the flow of the anolyte solution does not have as much influence on the corrosion front pathway. The primary determinant is the way the grain distinct layers are arranged and inclined, and the channelling path. In the AA2024-T3 alloy, the corrosion front pathway is also very much influenced by the flow of the anolyte solution. This is confirmed in Fig. 5 which displays the results of an SVET immersion test in the study of the galvanic interactions between AA2024-T3 and mild steel at a solution temperature of (45±2) °C in naturally aerated 3.5% NaCl solution. In the figure, the AA2024-T3 alloy is placed on the left and the mild steel alloy is placed on the right; also positive current density values represent anodic current density values whilst negative current density values represent cathodic current density values. Figures 5(a)−(d) show the SVET image maps of the galvanic couple after the 1st scan (scan 0), the 5th scan (scan 4), the 9th scan (scan 8) and the 13th scan (scan 12) respectively. The maps indicate a flow of anolyte solution in the corrosion front pathway as represented by the arrows. Figure 5(e) shows plots of the current density values for the scans 0, 4, 8, and 12, at the line designated by the arrows in Figs. 5(a)−(d) displaying increase in the anodic current density values at the mild steel region in contact with the AA2024-T3 alloy over time, and this is due to the flow of anolyte solution from the AA2024-T3 alloy. Figure 5(f) shows an optical micrograph of the AA2024-T3/mild steel couple after the SVET test displaying a preferentially corroded region in the mild steel due to flow of anolyte solution from the AA2024-T3 region. It can be seen from the map of the 1st scan (Fig. 5(a)) that immediately on immersion, intense corrosion activities start to occur at the extreme

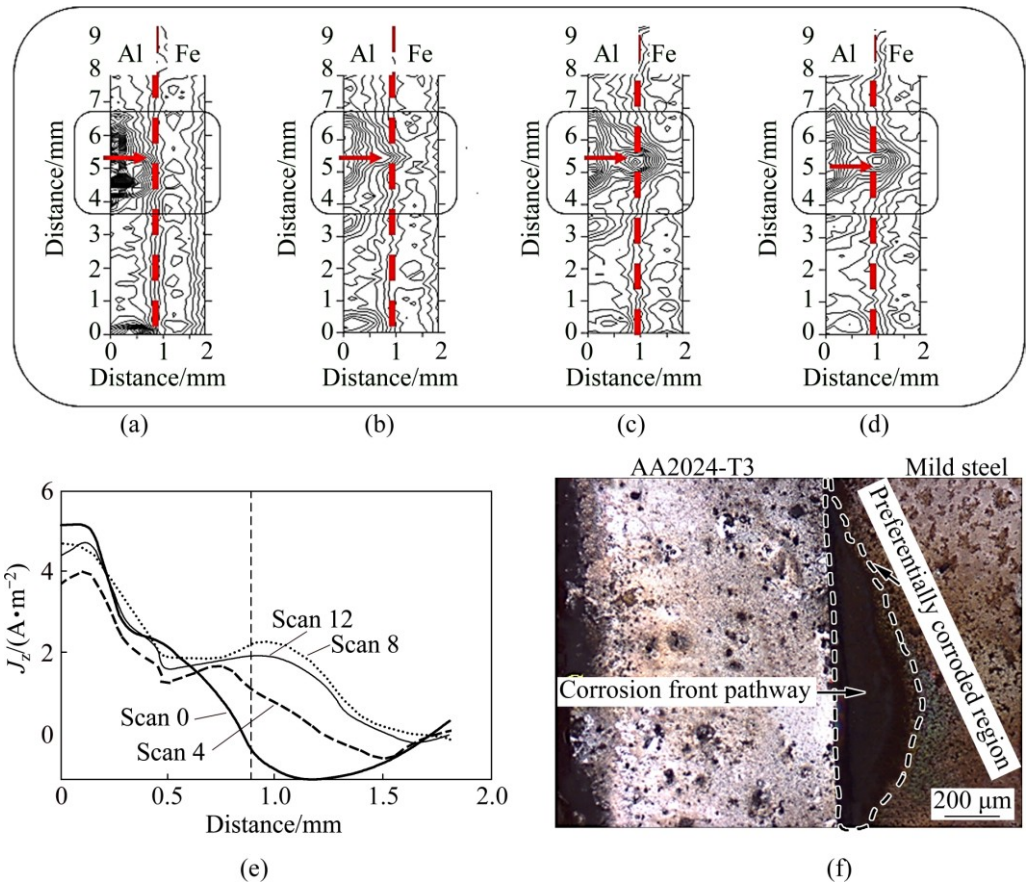

Fig. 5 SVET image maps of galvanic couple of AA2024-T3 alloy and mild steel after 1st scan (scan 0), 5th scan (scan 4), 9th scan (scan 8) and 13th scan (scan 12) respectively (a)−(d), at solution temperature of (45±2) °C in naturally aerated 3.5% NaCl solution, indicating flow of anolyte solution in corrosion front pathway as represented by arrows; (e) Plots of current density values for scans 0, 4, 8, and 12, at line designated by the arrows in (a)−(d), displaying increase in anodic current density values in mild steel region in contact with AA2024-T3 alloy due to flow of anolyte solution from AA2024-T3 alloy; (f) Optical micrograph of AA2024-T3/mild steel couple after SVET test displaying preferentially corroded region in mild steel due to flow of anolyte solution from AA2024-T3 region

left part of the AA2024-T3 alloy with intense cathodic activities on the mild steel (see the line plot for scan 0 in Fig. 5(e)). Over time, the intense corrosion activities spread rightward in the AA2024-T3 alloy and gradually into the mild steel alloy (Figs. 5(b)−(c)). This is evident in the line plots for scans 4, 8 and 12, where positive current density values are recorded on the mild steel alloy at the galvanic boundary. In addition to the line plot, the optical microscope (Fig. 5(f)) shows clearly that the spread in corrosion activities is as a result of the flow of anolyte solution and this dictated the corrosion front pathway.

4 Conclusions

The corrosion pathways in three different aluminium alloys (AA2024-T3, AA5083-O and AA6082-T6 alloys) have been studied and compared using the scanning electron micrographs of the alloys after potentiodynamic polarization tests in naturally aerated 3.5% NaCl solution. Corrosion propagates in two ways (particularly in the AA5083-O and AA6082-T6 alloys): an overall pathway in the corrosion front (filiform-like pathway in the AA5083 alloy and organized linear pathways in AA6082 alloy); and the crystallographic channelling along the ⟨100⟩ directions; all of which are primarily dependent on the grain distinct features of the alloys and are independent on the presence of coarse second phase particles. In the AA2024-T3 alloy, the corrosion mode is more second phase particles and grain boundary character dependent, and the corrosion front pathway also appears to be dependent on the grain distinct crystallographic details of the alloy. In addition, the flow of the anolyte solution plays a significant role in the corrosion front pathways since it causes the dissolution along it. However, it is not the primary factor in the corrosion front pathway of the AA6082-T6 alloy.

Acknowledgement

The authors wish to thank EPSRC for financial support through the LATEST2 Programme grant (EP/H020047/1), TWI for supply of materials and PTDF for supporting the studentship of Dr Uyime DONATUS during his PhD programme.

References

[1] ZHANG W, FRANKEL G. Localized corrosion growth kinetics in AA2024 alloys [J]. Journal of the Electrochemical Society, 2002, 149: 1−11.

[2] ILEVBARE G O, SCHNEIDER O, KELLY R G, SCULLY J R. In situ confocal laser scanning microscopy of AA 2024-T3 corrosion metrology [J]. Journal of the Electrochemical Society, 2007, 154(8): C397−C410.

[3] MA Y, ZHOU X, HUANG W, THOMPSON G E, ZHANG X, LUO C, SUN Z. Localized corrosion in AA2099-T83 aluminum–lithium alloy: The role of intermetallic particles [J]. Materials Chemistry and Physics, 2015, 161: 201−210.

[4] HASHIMOTO T, ZHOU X, LUO C, KAWANO K, THOMPSON G E, HUGHES A E, SKELDON P, WITHERS P J, MARROW T J, SHERRY A H. Nanotomography for understanding materials degradation [J]. Scripta Materialia, 2010, 63: 835−838.

[5] ZHOU X, LUO C, HASHIMOTO T, HUGHES A E, THOMPSON G E. Study of localized corrosion in AA2024 aluminium alloy using electron tomography [J]. Corrosion Science, 2012, 58: 299−306.

[6] DIMITROV N. Copper redistribution during corrosion of aluminum alloys [J]. Journal of the Electrochemical Society, 1999, 146: 98−102.

[7] SARVGHAD-MOGHADDAM M, PARVIZI R, DAVOODI A, HADDAD-SABZEVAR M, IMANI A. Establishing a correlation between interfacial microstructures and corrosion initiation sites in Al/Cu joints by SEM−EDS and AFM–SKPFM [J]. Corrosion Science, 2014, 79: 148−158.

[8] ANDREATTA F, TERRYN H, de WIT J H W. Corrosion behaviour of different tempers of AA7075 aluminium alloy [J]. Electrochimica Acta, 2004, 49: 2851−2862.

[9] XU W, LIU J, ZHU H. Pitting corrosion of friction stir welded aluminum alloy thick plate in alkaline chloride solution [J]. Electrochimica Acta, 2010, 55: 2918−2923.

[10] DONATUS U, THOMPSON G E, ZHOU X, WANG J, CASSELL A, BEAMISH K. Corrosion susceptibility of dissimilar friction stir welds of AA5083 and AA6082 alloys [J]. Materials Characterization, 2015, 107: 85−97.

[11] KING P, COLE I, CORRIGAN P, HUGHES A, MUSTER T. FIB/SEM study of AA2024 corrosion under a seawater drop: Part I [J]. Corrosion Science, 2011, 53: 1086−1096.

[12] HUGHES A, BOAG A, GLENN A. Corrosion of AA2024-T3 Part II: Co-operative corrosion [J]. Corrosion Science, 2011, 53: 27−39.

[13] BOAG A, MCCULLOCH D. Combined nuclear microprobe and TEM study of corrosion pit nucleation by intermetallics in aerospace aluminium alloys [J]. Nuclear Instruments and Methods, 2005, 231: 457−462.

[14] HUGHES A E, PARVIZI R, FORSYTH M. Microstructure and corrosion of AA2024 [J]. Corrosion Review, 2015, 33: 1−30.

[15] CAVANAUGH M K, LI J C, BIRBILIS N, BUCHHEIT R G. Electrochemical characterization of intermetallic phases common to aluminum alloys as a function of solution temperature [J]. Journal of The Electrochemical Society C, 2014, 161: 535−543.

[16] DONATUS U, THOMPSON G E, ZHOU X. Anodizing behavior of friction stir welded dissimilar aluminum alloys [J]. Journal of The Electrochemical Society C, 2015, 162: 657−665.

[17] IDRAC J, MANKOWSKI G, THOMPSON G, SKELDON P, KIHN Y, BLANC C. Galvanic corrosion of aluminium–copper model alloys [J]. Electrochimica Acta, 2007, 52: 7626−7633.

[18] GUILLAUMIN V, MANKOWSKI G. Localized corrosion of 6056 T6 aluminium alloy in chloride media [J]. Corrosion Science, 2000, 42: 105−125.

[19] LIU Z, CHONG P H, BUTT A N, SKELDON P, THOMPSON G E. Corrosion mechanism of laser-melted AA2014 and AA2024 alloys [J]. Applied Surface Science, 2005, 247: 294−299.

[20] BOAG A, HUGHES A, GLENN A. Corrosion of AA2024-T3 Part I: Localised corrosion of isolated IM particles [J]. Corrosion Science, 2011, 53: 17−26.

[21] YASAKAU K A, ZHELUDKEVICH M L, LAMAKA S V, FERREIRA M G S. Role of intermetallic phases in localized corrosion of AA5083 [J]. Electrochimica Acta, 2007, 52: 7651−7659.

[22] LUO C, ZHOU X, THOMPSON G E, HUGHES A E. Observations of intergranular corrosion in AA2024-T351: The influence of grain stored energy [J]. Corrosion Science, 2012, 61: 35−44.

[23] KIM S H, ERB U, AUST K T, PALUMBO G. Grain boundary character distribution and intergranular corrosion behavior in high purity aluminum [J]. Sripta Materialia, 2001, 44: 835−839.

[24] TAN L, ALLEN T R. Effect of thermomechanical treatment on the corrosion of AA5083 [J]. Corrosion Science, 2010, 52: 548−554.

[25] MINODA T, YOSHIDA H. Effect of grain boundary characteristics on intergranular corrosion resistance of 6061 aluminum alloy extrusion [J]. Metallurgical and Materials Transactions A, 2002, 33: 2891−2898.

[26] RALSTON KD, BIRBILIS N, DAVIES C H J. Revealing the relationship between grain size and corrosion rate of metals [J]. Scripta Materialia, 2010, 63: 1201−1204.

[27] RALSTON K D, BIRBILIS N. Effect of grain size on corrosion: A review [J]. Corrosion, 2010, 66: 0750051−07500513.

[28] DONATUS U, THOMPSON G E, LIU H, ZHOU X, LIU Z. Understanding the galvanic interactions between AA2024T3 and mild steel using the scanning vibrating electrode technique [J]. Materials Chemistry and Physics, 2015, 161: 228−236.

[29] NEWMAN R. Local chemistry considerations in the tunnelling corrosion of aluminium [J]. Corrosion Science, 1995, 37: 527−533.

[30] BAUMGÄRTNER M, KAESCHE H. Aluminum pitting in chloride solutions: Morphology and pit growth kinetics [J]. Corrosion Science, 1990, 3: 231−236.

[31] DONATUS U, THOMPSON G E, ELABAR D, HASHIMOTO T, MORSCH S. Features in aluminium alloy grains and their effects on anodizing and corrosion [J]. Surface and Coatings Technology, 2015, 277: 91−98.

[32] GLENN A, MUSTER T, LUO C, ZHOU X. Corrosion of AA2024-T3 Part III: Propagation [J]. Corrosion Science, 2011, 53: 40−50.

铝合金的腐蚀路径

U. DONATUS[1,2], G. E. THOMPSON[1], J. A. OMOTOYINBO[2],
K. K. ALANEME[2], S. ARIBO[2], O. G. AGBABIAKA[2]

1. School of Materials, The University of Manchester, Manchester M13 9PL, England, UK;
2. Department of Metallurgical and Materials Engineering, Federal University of Technology,
Akure, PMB 704, Akure, Ondo State, Nigeria

摘　要：研究 AA2024-T3、AA5083-O 和 AA6082-T6 合金的腐蚀路径，以进一步了解铝合金局部腐蚀机理。采用扫插电子显微镜研究合金在 3.5% NaCl 溶液中动电位极化测试后腐蚀表面，利用扫描振动电极技术分析阳极电解液的流动。结果表明：各合金的腐蚀路径明显不同，且受阳极电解液流动的影响。另外，在 AA5083-O 和 AA6082 合金中，腐蚀以两种方式进行扩展：一种为腐蚀前端扩展路径(AA5083 的丝状扩展路径和 AA6082 合金有条理的线性扩散路径)；另一种为沿⟨100⟩方向的晶体学通道扩展路径。与 AA2024-T3 合金相比，AA5083-O 和 AA6082-T6 合金的扩展路径与晶粒特征有关，而与粗大的第二相粒子无关。而 AA2024-T3 的扩展路径与第二相粒子和晶界特征有关。

关键词：腐蚀前端路径；晶体学通道；阳极电解液流动；铝合金

(Edited by Yun-bin HE)